

# Planck 2015

## Part 2 : Power spectra, Likelihoods & Parameters

Jayanti Prasad  
IUCAA/CMS (Pune University), Pune

October 12, 2015

## Summary

- The most important result of Planck 2013 was the finding that simple, single field inflationary models with a tilted scalar spectral index,  $n_s = 0.96$ , provide the very good fit to the Planck data.
- Planck 2015 finds no evidence for tensor perturbations, running, isocurvature perturbations, features in the primordial power spectrum, cosmic strings, non-Gaussianity etc.
- On large angular scales Planck also shows anomalies, as seen in WMAP9 , including a dip in  $C_l$  in the range  $20 \leq l \leq 30$  and some evidence for departure from statistically isotropy at large angular scales.
- The statistical significance for the anomalies found by Planck (as discussed above) is not strong enough.

# Important results

- Constraints on scalar spectral index  $n_s$  and tensor-to-scalar ration  $r$ .
- Curvature  $\Omega_k$ .
- Iso-curvature perturbations
- Dark energy
- Neutrinos :  $N_{\text{eff}}$ ,  $\sum m_\nu$ .
- Dark matter annihilation rate ..

# Power Spectra & Likelihoods

- The CMB power spectra  $C_l^{XY}$  where  $X, Y = T, E, B$  contain all of the information available if the CMB is statistically isotropic and Gaussian.
- CMB power spectra are uniquely determined by the underlying cosmological model and its parameters.
- Planck maps consist of the order  $5 \times 10^7$  pixels for each detector so pixel based likelihood will be computationally expansive.
- Planck follows a hybrid approach - likelihood at low- $l$  is directly computed in the pixel space and at high- $l$  Pseudo- $C_l$  approach is used which approximate likelihood in a Gaussian form.

# Power Spectra & Likelihoods

- At low- $\ell$  commander (which is a Bayesian Monte Carlo method which samples from or maximize a global posterior defined by some explicit parametric model and a set of parameters) is used for component separation.
- Commander analysis allows us to separate low-frequency foregrounds into separate synchrotron, free-free and spinning dust components as well as to constrain the thermal dust temperature pixel by pixel.
- At high- $\ell$  Planck likelihood is based on Pseudo  $C_\ell$  computed from HFI data, as well as further parameters describing the contribution of foregrounds and instrumental effects.

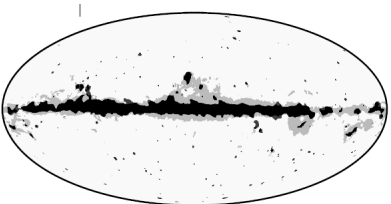
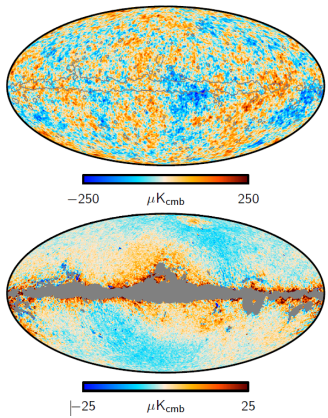
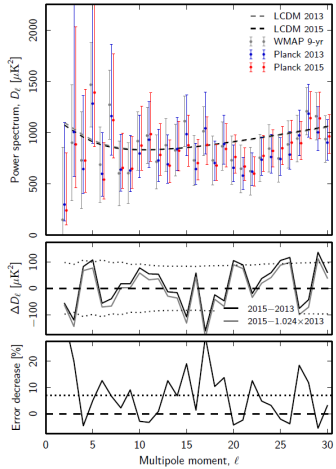


**Figure 1.** Top: Commander CMB temperature map derived from the *Planck* 2015, 9-year WMAP, and 408 MHz Haslam et al. observations, as described in [Planck Collaboration X \(2015\)](#). The gray boundary indicates the 2015 likelihood temperature mask, covering a total of 7 % of the sky. The masked area has been filled with a constrained Gaussian realization. Middle: difference between the 2015 and 2013 Commander temperature maps. The masked region indicates the 2013 likelihood mask, removing 13 % of the sky. Bottom: comparison of the 2013 (gray) and 2015 (black) temperature likelihood masks.



multipole moment,  $\ell$

**Figure 2.** *Top:* comparison of the *Planck* 2013 (blue points) and 2015 (red points) posterior-maximum low- $\ell$  temperature power spectra, as derived with Commander. Error bars indicate asymmetric marginal posterior 68 % confidence regions. For reference, we also show the final 9-year WMAP temperature spectrum in light gray points, as presented by Bennett et al. (2013); note that the error bars indicate symmetric Fisher uncertainties in this case. The dashed lines show the best-fit  $\Lambda$ CDM spectra derived from the respective data sets, including high-multipole and polarization information. *Middle:* difference between the 2015 and 2013 maximum-posterior power spectra (solid black line). The gray shows the same difference after scaling the 2013 spectrum up by 2.4 %. Dotted lines indicate the expected  $\pm 1\sigma$  confidence region, accounting only for the sky fraction difference. *Bottom:* reduction in marginal error bars between the 2013 and 2015 temperature spectra; see main text for explicit definition. The dotted line shows the reduction expected from increased sky fraction alone.

**Table 1.** Likelihood codes and datasets. We use these designations throughout the text to refer to specific likelihood codes and implementations that use different input data.

Name	Description
PlanckTT . . . . .	Full <i>Planck</i> temperature-only $C_\ell^{TT}$ likelihood
PlanckTT,TE,EE . . . . .	PlanckTT combined with high- $\ell$ $C_\ell^{TE} + C_\ell^{EE}$ likelihood
lowP . . . . .	Low- $\ell$ polarization $C_\ell^{TE} + C_\ell^{EE} + C_\ell^{BB}$ likelihood
lowTEB . . . . .	Low- $\ell$ temperature-plus-polarization likelihood
PlikTT . . . . .	High- $\ell$ $C_\ell^{TT}$ -only likelihood
PlikEE . . . . .	High- $\ell$ $C_\ell^{EE}$ -only likelihood
PlikTE . . . . .	High- $\ell$ $C_\ell^{TE}$ -only likelihood
PlikTT,TE,EE . . . . .	High- $\ell$ $C_\ell^{TT} + C_\ell^{TE} + C_\ell^{EE}$ likelihood
Plik_lite . . . . .	High- $\ell$ $C_b^{TT} + C_b^{TE} + C_b^{EE}$ , foreground-marginalized bandpower likelihood
tauprior . . . . .	Gaussian prior, $\tau = 0.07 \pm 0.02$
highL . . . . .	ACT+SPT high- $\ell$ likelihood
WP . . . . .	WMAP low- $\ell$ polarization likelihood <sup>a</sup>

<sup>a</sup> Note that “low- $\ell$ ” refers to  $\ell < 23$  for WP, but  $\ell < 30$  for the *Planck* likelihoods.

# Low-l information

- Cosmological parameters which are most sensitive to CMB power at low-l are the reionization optical depth  $\tau$ , the scalar amplitude  $A_s$  and the tensor to scalar ratio  $r$ .
- Low-l temperature mainly contains information on the combination  $A_s e^{-2\tau}$ , at least at multipoles corresponding to an angular scale smaller than the scale subtended by the horizon at reionization.
- The lowest temperature multipoles are directly sensitive to  $A_s$ .
- Low-l polarization power is sensitive to the combination  $A_s \tau^2$  so neither low-l temperature nor polarization can separately constrain  $\tau$  and  $A_s$ .

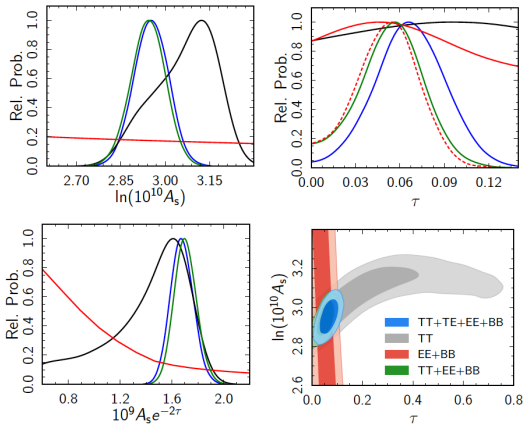


**Figure 6.** Likelihoods for parameters from low- $\ell$  data. *Panels 1–3:* One-dimensional posteriors for  $\log[10^{10} A_s]$ ,  $\tau$ , and  $A_s e^{-2\tau}$  for the several sub-blocks of the likelihood, for cases 1 (blue), 2 (black), 3 (red), and 4 (green) – see text for definitions; dashed red is the same as case 3 but imposes a sharp prior  $10^9 A_s e^{-2\tau} = 1.88$ . *Panel 4:* Two-dimensional posterior for  $\log[10^{10} A_s]$  and  $\tau$  for the same data combinations; shading indicates the 68 % and 95 % confidence regions.

**Table 2.** Parameters estimated from the low- $\ell$  likelihood.<sup>a</sup>

Parameter	$\Lambda$ CDM	$\Lambda$ CDM+ $r$
$\tau$ . . . . .	$0.067 \pm 0.023$	$0.064 \pm 0.022$
$\log[10^{10}A_s]$ . . . .	$2.952 \pm 0.055$	$2.788_{-0.09}^{+0.19}$
$r$ . . . . .	0	[0, 0.90]
$z_{\text{re}}$ . . . . .	$8.9_{-2.0}^{+2.5}$	$8.5_{-2.1}^{+2.5}$
$10^9 A_s$ . . . . .	$1.92_{-0.12}^{+0.10}$	$1.64_{-0.17}^{+0.29}$
$A_s e^{-2\tau}$ . . . . .	$1.675_{-0.093}^{+0.082}$	$1.45_{-0.14}^{+0.24}$

<sup>a</sup> For the centre column the set of parameters  $(\tau, A_s)$  was sampled, while it was the set  $(\tau, A_s, r)$  for the right column. Unsampled parameters are fixed to their  $\Lambda$ CDM 2015 best-fit fiducial values. All errors are 68 % CL (confidence level), while the upper limit on  $r$  is 95 %. The bottom portion of the table shows a few additional derived parameters for information.

# High-l Likelihood

- At high-l Planck likelihood is based on Pseudo  $C_l$  computed from HFI data, as well as further parameters describing the contribution of foregrounds and instrumental effects.
- As compared to 2013, Planck 2015 analysis includes the use of polarization data at high-l with more detailed model of foregrounds and instruments.
- For a single power spectrum the likelihood for each multipole  $l$  simplifies to an inverse  $\chi^2$  distribution with  $(2l + 1)$  degrees of freedom. At large enough  $l$ , the central limit theorem ensures that the shape of the likelihood is very close to Gaussian.

$$-\ln \mathcal{L}(\hat{C}, C(\theta)) = \frac{1}{2} [\hat{C} - C(\theta)]^T C^{-1} [\hat{C} - C(\theta)] + \text{const} \quad (1)$$

# High-l Likelihood: Model & Data

The model vector  $\mathbf{C}(\theta)$  must represent the content of the data vector. It can be written schematically as

$$\begin{aligned} C_{\nu \times \nu'}^{\text{XY}}|_{\ell}(\theta) &= M_{\text{ZW}, \nu \times \nu'}^{\text{XY}}|_{\ell}(\theta_{\text{inst}}) C_{\nu \times \nu'}^{\text{ZW,sky}}|_{\ell}(\theta) + N_{\nu \times \nu'}^{\text{XY}}|_{\ell}(\theta_{\text{inst}}), \\ C_{\nu \times \nu'}^{\text{ZW,sky}}|_{\ell}(\theta) &= C^{\text{ZW,cmb}}|_{\ell}(\theta) + C_{\nu \times \nu'}^{\text{ZW,fg}}|_{\ell}(\theta), \end{aligned} \quad (14)$$

where  $C_{\nu \times \nu'}^{\text{XY}}|_{\ell}(\theta)$  is the element of the model vector corresponding to the multipole  $\ell$  of the XY cross-spectra ( $X$  and  $Y$  being either  $T$  or  $E$ ) between the pair of frequencies  $\nu$  and  $\nu'$ . This element of the model originates from the sum of the microwave emission of the sky, i.e., the CMB ( $C^{\text{ZW,cmb}}|_{\ell}(\theta)$ ) which does not depend of the pair of frequencies (all maps are in units of  $K_{\text{cmb}}$ ), and foreground ( $C_{\nu \times \nu'}^{\text{ZW,fg}}|_{\ell}(\theta)$ ). Section 3.3 will describe the foreground modelling. The mixing matrix  $M_{\text{ZW}, \nu \times \nu'}^{\text{XY}}|_{\ell}(\theta_{\text{inst}})$  accounts for imperfect calibration, imperfect beam correction, and possible leakage between temperature and polarization. It does depend on the pair of frequencies and can depend on the multipole when accounting for imperfect beams and leakages. Finally, the noise term  $N_{\nu \times \nu'}^{\text{XY}}|_{\ell}(\theta_{\text{inst}})$  accounts for the possible correlated noise in the XY cross-spectra for the pair of frequencies  $\nu \times \nu'$ . Sections 3.2.3 and 3.4 will describe our instrument model.

## 3.2. Data

The data vector  $\hat{\mathbf{C}}$  in the likelihood equation (Eq. 13) is constructed from concatenated temperature and polarization components,

$$\hat{\mathbf{C}} = (\hat{\mathbf{C}}^{TT}, \hat{\mathbf{C}}^{EE}, \hat{\mathbf{C}}^{TE}), \quad (15)$$

which in turn comprise the following frequency-averaged spectra:

$$\hat{\mathbf{C}}^{TT} = (\hat{\mathbf{C}}^{TT}_{100 \times 100}, \hat{\mathbf{C}}^{TT}_{143 \times 143}, \hat{\mathbf{C}}^{TT}_{143 \times 217}, \hat{\mathbf{C}}^{TT}_{217 \times 217}) \quad (16)$$

$$\hat{\mathbf{C}}^{EE} = (\hat{\mathbf{C}}^{EE}_{100 \times 100}, \hat{\mathbf{C}}^{EE}_{100 \times 143}, \hat{\mathbf{C}}^{EE}_{100 \times 217}, \hat{\mathbf{C}}^{EE}_{143 \times 143}, \hat{\mathbf{C}}^{EE}_{143 \times 217}, \hat{\mathbf{C}}^{EE}_{217 \times 217}) \quad (17)$$

$$\hat{\mathbf{C}}^{TE} = (\hat{\mathbf{C}}^{TE}_{100 \times 100}, \hat{\mathbf{C}}^{TE}_{100 \times 143}, \hat{\mathbf{C}}^{TE}_{100 \times 217}, \hat{\mathbf{C}}^{TE}_{143 \times 143}, \hat{\mathbf{C}}^{TE}_{143 \times 217}, \hat{\mathbf{C}}^{TE}_{217 \times 217}). \quad (18)$$

# Planck $C_\ell$ s

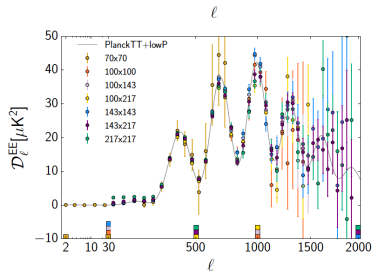
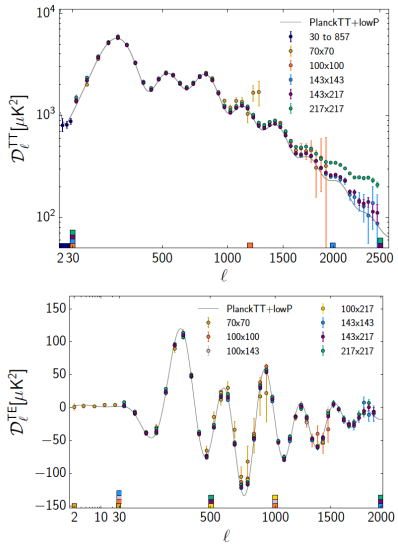


**Figure 15.** *Planck* power spectra (not yet corrected for foregrounds and data selection). The coloured tick marks indicate the  $\ell$ -range of the cross-spectra included in the *Planck* likelihood. Although not used in the high- $\ell$  likelihood, the 70 GHz spectra at  $\ell > 29$  illustrate the consistency of the data. The grey line indicates the best-fit *Planck* 2015 spectrum. Note that the  $TE$  and  $EE$  plots have a logarithmic horizontal scale for  $\ell < 30$ .

# Foregrounds Modeling

- Galactic dust is the main foreground contribution at large scales.
- The dust contribution to the power spectrum calculated from the map  $X$  at frequency  $\nu$  and map  $Y$  at frequency map  $\nu'$  is given by:

$$\left( X_{\nu,\nu'}^{X,Y,dust} \right)_l = A_{\nu,\nu'}^{X,Y,dust} \times C_l^{X,Y,dust} \quad (2)$$

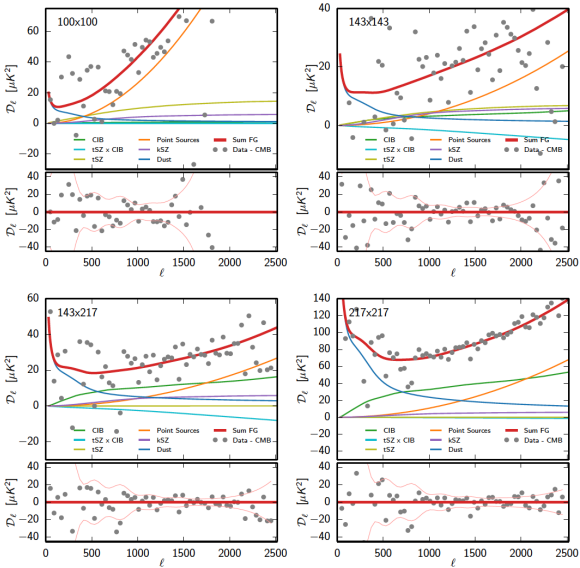


**Figure 16.** Best foreground model in each of the cross-spectra used for the temperature high- $\ell$  likelihood. The data corrected by the best theoretical CMB  $C_\ell$  are shown in grey. The bottom panel of each plot shows the residual after foreground correction. The pink line shows the  $1\sigma$  value from the diagonal of the covariance matrix (32 % of the unbinned points are out of this range).

**Table 9.** Parameters used for astrophysical foregrounds and instrumental modelling.<sup>a</sup>

Parameter	Prior range	Definition
$A_{100}^{\text{PS}}$ . . . . .	[0, 400]	Contribution of Poisson point-source power to $\mathcal{D}_{3000}^{100 \times 100}$ for <i>Planck</i> (in $\mu\text{K}^2$ )
$A_{143}^{\text{PS}}$ . . . . .	[0, 400]	As for $A_{100}^{\text{PS}}$ but at 143 GHz
$A_{217}^{\text{PS}}$ . . . . .	[0, 400]	As for $A_{100}^{\text{PS}}$ but at 217 GHz
$A_{143 \times 217}^{\text{PS}}$ . . . . .	[0, 400]	As for $A_{100}^{\text{PS}}$ but at $143 \times 217$ GHz
$A_{217}^{\text{CIB}}$ . . . . .	[0, 200]	Contribution of CIB power to $\mathcal{D}_{3000}^{217}$ at the <i>Planck</i> CMB frequency for 217 GHz (in $\mu\text{K}^2$ )
$A^{\text{tSZ}}$ . . . . .	[0, 10]	Contribution of tSZ to $\mathcal{D}_{3000}^{143 \times 143}$ at 143 GHz (in $\mu\text{K}^2$ )
$A^{\text{kSZ}}$ . . . . .	[0, 10]	Contribution of kSZ to $\mathcal{D}_{3000}$ (in $\mu\text{K}^2$ )
$\xi^{\text{tSZ} \times \text{CIB}}$ . . . . .	[0, 1]	Correlation coefficient between the CIB and tSZ
$A_{100}^{\text{dust}TT}$ . . . . .	[0, 50] (7 ± 2)	Amplitude of Galactic dust power at $\ell = 200$ at 100 GHz (in $\mu\text{K}^2$ )
$A_{143}^{\text{dust}TT}$ . . . . .	[0, 50] (9 ± 2)	As for $A_{100}^{\text{dust}TT}$ but at 143 GHz
$A_{143 \times 217}^{\text{dust}TT}$ . . . . .	[0, 100] (21 ± 8.5)	As for $A_{100}^{\text{dust}TT}$ but at $143 \times 217$ GHz
$A_{217}^{\text{dust}TT}$ . . . . .	[0, 400] (80 ± 20)	As for $A_{100}^{\text{dust}TT}$ but at 217 GHz
$c_{100}$ . . . . .	[0, 3] (0.9990004 ± 0.001)	Power spectrum calibration for the 100 GHz
$c_{217}$ . . . . .	[0, 3] (0.99501 ± 0.002)	Power spectrum calibration for the 217 GHz
$y_{\text{cal}}$ . . . . .	[0.9, 1.1] (1 ± 0.0025)	Absolute map calibration for <i>Planck</i>

$A_{100}^{\text{dust}EE}$	[0, 10] (0.06 ± 0.012)	Amplitude of Galactic dust power at $\ell = 500$ at 100 GHz (in $\mu\text{K}^2$ )
$A_{100 \times 143}^{\text{dust}EE}$	[0, 10] (0.05 ± 0.015)	As for $A_{100}^{\text{dust}EE}$ but at $100 \times 143$ GHz
$A_{100 \times 217}^{\text{dust}EE}$	[0, 10] (0.11 ± 0.033)	As for $A_{100}^{\text{dust}EE}$ but at $100 \times 217$ GHz
$A_{143}^{\text{dust}EE}$	[0, 10] (0.1 ± 0.02)	As for $A_{100}^{\text{dust}EE}$ but at 143 GHz
$A_{143 \times 217}^{\text{dust}EE}$	[0, 10] (0.24 ± 0.048)	As for $A_{100}^{\text{dust}EE}$ but at $143 \times 217$ GHz
$A_{217}^{\text{dust}EE}$	[0, 10] (0.72 ± 0.14)	As for $A_{100}^{\text{dust}EE}$ but at 217 GHz
$A_{100}^{\text{dust}TE}$	[0, 10] (0.14 ± 0.042)	Amplitude of Galactic dust power at $\ell = 500$ at 100 GHz (in $\mu\text{K}^2$ )
$A_{100 \times 143}^{\text{dust}TE}$	[0, 10] (0.12 ± 0.036)	As for $A_{100}^{\text{dust}TE}$ but at $100 \times 143$ GHz
$A_{100 \times 217}^{\text{dust}TE}$	[0, 10] (0.3 ± 0.09)	As for $A_{100}^{\text{dust}TE}$ but at $100 \times 217$ GHz
$A_{143}^{\text{dust}TE}$	[0, 10] (0.24 ± 0.072)	As for $A_{100}^{\text{dust}TE}$ but at 143 GHz
$A_{143 \times 217}^{\text{dust}TE}$	[0, 10] (0.6 ± 0.18)	As for $A_{100}^{\text{dust}TE}$ but at $143 \times 217$ GHz
$A_{217}^{\text{dust}TE}$	[0, 10] (1.8 ± 0.54)	As for $A_{100}^{\text{dust}TE}$ but at 217 GHz

The columns indicate the symbol for each parameter, the prior used for exploration (square brackets denote uniform priors, parentheses indicate Gaussian priors), and definitions. Note that beam eigenmode amplitudes require a correlation matrix to fully describe their joint prior and so do not appear in the table; they are internally marginalized over rather than explicitly sampled. This table only lists the instrumental parameters that are explored in the released version, but we do consider more parameters to assess the effects of beam uncertainties and beam leakage; see Sect. 3.4.3.

**Point sources.** At the likelihood level, we cannot differentiate between the radio- and IR-point sources. We thus describe their combined contribution by their total emissivity per frequency pair,

$$\left(C_{\nu\nu'}^{\text{PS}}\right)_{\ell} = \mathcal{D}_{\nu\nu'}^{\text{PS}} / \mathcal{A}_{3000}, \quad (27)$$

where  $\mathcal{D}_{\nu\nu'}$  is the amplitude of the point-source contribution in  $\mathcal{D}_{\ell}$  at  $\ell = 3000$ . Note that, contrary to 2013, we do not use a correlation parameter to represent the  $143 \times 217$  point-source contribution; instead we use a free amplitude parameter. This has the disadvantage of not preventing a possible unphysical solution. However, it simplifies the parameter optimization, and it is easier to understand in terms of contamination amplitude.

**Kinetic SZ (kSZ).** We use the same model as in 2013. The kSZ emission is parameterized with a single amplitude and a fixed template from [Trac et al. \(2011\)](#),

$$\left(C_{\nu\nu'}^{\text{kSZ}}\right)_{\ell} = C_{\ell}^{\text{kSZ}} \times \mathcal{D}^{\text{kSZ}}, \quad (28)$$

where  $\mathcal{D}^{\text{kSZ}}$  is the kSZ contribution at  $\ell = 3000$ .

**Thermal SZ (tSZ).** Here again, we use the same model as in 2013. The tSZ emission is also parameterized by a single amplitude and a fixed template using the  $\epsilon = 0.5$  model from

[Efstathiou & Migliaccio \(2012\)](#),

$$\left(C_{\nu\nu'}^{\text{tSZ}}\right)_{\ell} = a_{\nu}^{\text{tSZ}} a_{\nu'}^{\text{tSZ}} C_{\ell}^{\text{tSZ}} \times \mathcal{D}_{143}^{\text{tSZ}}, \quad (29)$$

where  $a_{\nu}^{\text{tSZ}}$  is the thermal Sunyaev-Zeldovich spectrum, normalized to  $\nu_0 = 143$  GHz and corrected for the *Planck* bandpass colour corrections. Ignoring the bandpass correction, we recall that the tSZ spectrum is given by

$$a_{\nu}^{\text{tSZ}} = \frac{f(\nu)}{f(\nu_0)}, \quad f(\nu) = \left( x \coth\left(\frac{x}{2}\right) - 4 \right), \quad x = \frac{h\nu}{k_B T_{\text{cmb}}}. \quad (30)$$

**Thermal SZ  $\times$  CIB correlation.** Following [Like13](#) the cross-correlation between the thermal SZ and the CIB, tSZ  $\times$  CIB, is parameterized by a single correlation parameter,  $\xi$ , and a fixed template from [Addison et al. \(2012\)](#),

$$\begin{aligned} \left(C_{\nu\nu'}^{\text{tSZ}\times\text{CIB}}\right)_{\ell} &= \xi \sqrt{\mathcal{D}_{143}^{\text{tSZ}} \mathcal{D}_{217}^{\text{CIB}}} \\ &\times \left( a_{\nu}^{\text{tSZ}} a_{\nu'}^{\text{CIB}} + a_{\nu'}^{\text{tSZ}} a_{\nu}^{\text{CIB}} \right) \\ &\times C_{\ell}^{\text{tSZ}\times\text{CIB}}, \end{aligned} \quad (31)$$

where  $a_{\nu}^{\text{tSZ}}$  is the thermal Sunyaev-Zeldovich spectrum, corrected for the *Planck* bandpass colour corrections and  $a_{\nu}^{\text{CIB}}$  is the CIB spectrum, rescaled at  $\nu = 217$  GHz as in the previous paragraphs.

# High-l likelihood: CamSpec

- Let us define  $\tilde{T}_{lm}^i$  as the spherical harmonic coefficients of the weighted temperature map of detector  $i$ . The pseudo spectrum at multipole  $l$ , for the detector pair  $(i,j)$ , is then given by:

$$\tilde{C}_l^{ij} = \frac{1}{2l+1} \sum_m \tilde{T}_{lm}^i \tilde{T}_{lm}^{j\dagger} \quad (3)$$

- The pseudo- $C_l$  is related to the “deconvolved”  $\hat{C}_{ij}^T$  in the following way:

$$\tilde{C}_{ij}^T = M_{ij}^{TT} \hat{C}_{ij}^T, \quad (4)$$

where  $M$  is the coupling matrix.

- The likelihood can be defined as  $e^{-S}$  with :

$$S = \frac{1}{2}(\hat{\mathbf{X}} - \mathbf{X})^T \hat{M}^{-1}(\hat{\mathbf{X}} - \mathbf{X}), \quad (5)$$

where  $\hat{\mathbf{X}} = \text{Vec}(\hat{C})$  and

$$\hat{M} = (\hat{\mathbf{X}} - \mathbf{X})(\hat{\mathbf{X}} - \mathbf{X})^T \quad (6)$$

- For 2013, analysis :

$$\hat{\mathbf{X}} = \left( \hat{C}_I^{100 \times 100}, \hat{C}_I^{143 \times 143}, \hat{C}_I^{217 \times 217}, \hat{C}_I^{143 \times 217} \right) \quad (7)$$

# High-l likelihood Plik

## 2.2. The Plik likelihood

We now describe the alternative form of the likelihood, inspired by [Cardoso et al. \(2008\)](#), used for cross-checks and robustness tests. We start from the full-sky exact likelihood for a Gaussian signal, which for  $N_{\text{map}}$  detector maps is given by

$$p(\text{maps}|\theta) \propto \exp - \left\{ \sum_{\ell} (2\ell + 1) \mathcal{K}(\hat{\mathbf{C}}_{\ell}, \mathbf{C}_{\ell}(\theta)) \right\},$$

where  $\theta$  is a vector containing the parameters of the signal model, and  $\hat{\mathbf{C}}_{\ell}$  are the empirical angular spectra.  $\mathcal{K}(\mathbf{A}, \mathbf{B})$  denotes the Kullback divergence between two  $n$ -variate zero-mean Gaussian distributions with covariance matrices  $\mathbf{A}$  and  $\mathbf{B}$ , and is given by

$$\mathcal{K}(\mathbf{A}, \mathbf{B}) = \frac{1}{2} [\text{tr}(\mathbf{AB}^{-1}) - \log \det(\mathbf{AB}^{-1}) - n].$$

As already noted, a sky cut introduces off-diagonal couplings between different multipoles. In this method we bin the power spectra in such a way that these off-diagonal terms of the covariance are negligible. This is adequate to model sources with slowly varying spectra, such as foregrounds, and the CMB anisotropies for standard cosmologies. In this case, the likelihood takes the form

$$p(\text{maps}|\theta) \propto \exp - \mathcal{L}(\theta), \quad \text{with} \quad \mathcal{L}(\theta) = \sum_{q=1}^Q n_q \mathcal{K}(\hat{\mathbf{C}}_q, \mathbf{C}_q), \quad (6)$$

where the angular spectra  $\hat{\mathbf{C}}_{\ell}$  for each cross-frequency spectrum have been averaged into  $Q$  spectral bins using spectral windows  $w_q(\ell)$  ( $q = 1, \dots, Q$ ), with

$$\hat{\mathbf{C}}_q = \sum_{\ell} w_q(\ell) \ell \hat{\mathbf{C}}_{\ell}, \quad \mathbf{C}_q = \sum_{\ell} w_q(\ell) \mathbf{C}_{\ell}.$$

Here  $w_q(\ell)$  denotes the window function for the  $q$ th bin, and the same symbol,  $\mathbf{C}$ , is used to denote binned or unbinned spectra. The effective number of modes in the  $q$ th bin is

$$n_q = f_{\text{sky}} \cdot \frac{(\sum_{\ell} w_q(\ell)^2)^2}{\sum_{\ell} w_q(\ell)^4 / (2\ell + 1)}.$$

We adopt a spectral binning defined by

$$w_q(\ell) = \begin{cases} \frac{\ell(\ell+1)(2\ell+1)}{\sum_{\ell_{\min}}^{\ell_{\max}} \ell(\ell+1)(2\ell+1)} & \ell_{\min}^q \leq \ell \leq \ell_{\max}^q, \\ 0 & \text{otherwise.} \end{cases}$$

The Plik bin width is  $\Delta\ell = 9$  from  $\ell = 100$  to  $\ell = 1503$ , then  $\Delta\ell = 17$  to  $\ell = 2013$ , and finally  $\Delta\ell = 33$  to  $\ell_{\max} = 2508$ . This ensures that correlations between any two bins are smaller than 10%.

While this binned likelihood approximation does not fully capture all couplings between different multipoles, it has a notable advantage in computational speed, and it agrees well with the primary likelihood. It is therefore very well suited for performing an extensive suite of robustness tests, as many more parameters can be considered in a short time. Further, instrumental effects can be investigated quickly to assess the agreement between pairs of detectors within a frequency channel, such as individual detector calibrations and beam errors.

# High-l likelihood Plik

A specific example is the impact of (effective) beam uncertainty parameters on the likelihood. This can be investigated by re-expressing the model covariance matrices as

$$\mathbf{C}_\ell = \mathbf{B}_\ell(\gamma) \mathbf{C}_\ell(\theta) \mathbf{B}_\ell(\gamma)^T, \quad (7)$$

where  $\mathbf{C}_\ell(\theta)$  is the model covariance including both signal and noise, and  $\mathbf{B}_\ell(\gamma)$  is a diagonal matrix encoding the beam and calibration errors with elements given by<sup>2</sup>

$$B_\ell^i(\gamma) = \exp \left( \sum_{k=1}^{n_{\text{modes}}} \delta_k^i E_k^{\bar{i}}(\ell) \right). \quad (8)$$

Here,  $E_k^{\bar{i}}(\ell)$  are the eigenmodes of the (auto-)spectra, similar to Eq. (5). Note that Eq. (7) does not contain the *mean* beam transfer function, since it is already included in the empirical spectra. Thus, using Eq. (7) Plik approximates the cross-spectrum beam errors as the harmonic mean of the corresponding auto-spectrum beam errors, under the assumption that  $\mathbf{B}_\ell$  is diagonal between detectors. This approximate factorisation is intrinsically linked to the assumed Kullback shape of the Plik likelihood, and is later demonstrated to work well for both simulations and data.

<sup>2</sup> From Eqs. (5), (7), and (8), we have  $\delta_k^i = g_k^{\bar{i}}/2$  at first order.

The Plik likelihood method also provides a direct estimate of the detector noise power spectra as it can include the empirical auto-spectra, and we find that these noise estimates are in good agreement with the noise spectra used to construct the CamSpec likelihood covariance matrix. The method can also produce a binned CMB power spectrum independent of the underlying cosmological model, providing a direct quality assessment of the foreground model parametrisation. In practice, we proceed in two steps. First, we jointly estimate the noise together with all other parameters using both auto and cross-spectra. Then we fix the noise estimates, and use the fiducial Gaussian approximation to explore the remaining free parameters excluding the auto-spectra, optionally including only specific data combinations.

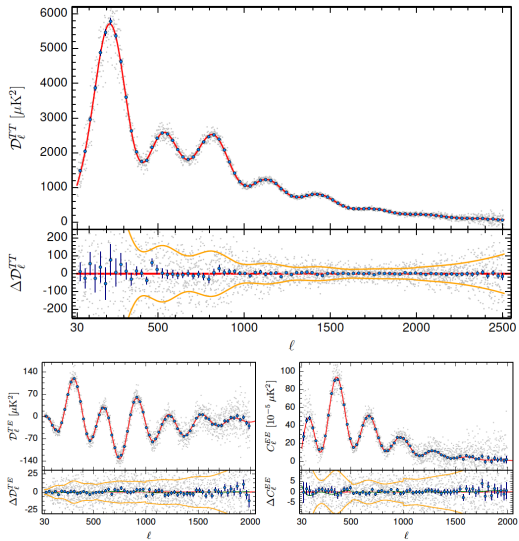


**Figure 26.** Plik 2015 co-added  $TT$ ,  $TE$ , and  $EE$  spectra. The blue points are for bins of  $\Delta\ell = 30$ , while the grey points are unbinned. The lower panels show the residuals with respect to the best fit PlikTT+tauprior  $\Lambda$ CDM model. The yellow lines show the 68 % unbinned error bars. For  $TE$  and  $EE$ , we also show the best-fit beam-leakage correction (green line; see text and Fig. 21).

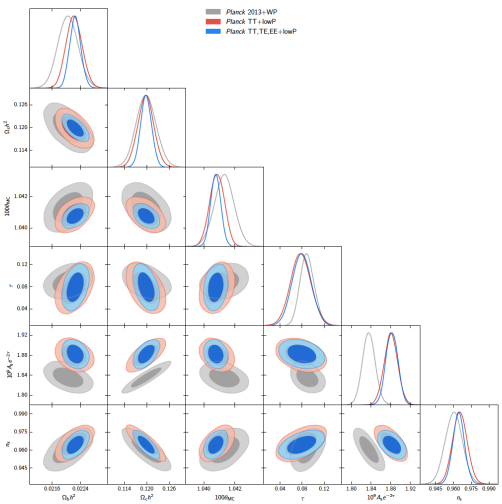
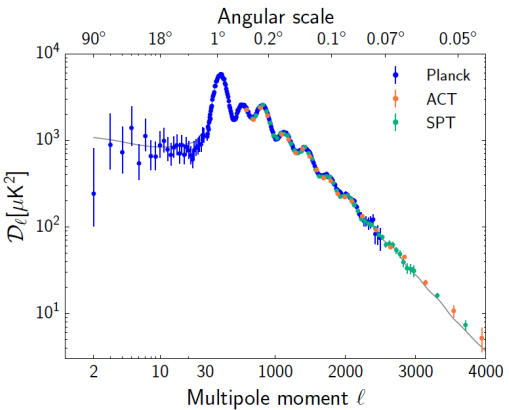


Figure 41.  $\Lambda$ CDM parameter constraints. The grey contours show the 2013 constraints, which can be compared with the current ones, using either  $TT$  only at high  $\ell$  (red) or the full likelihood (blue). Apart from further tightening, the main difference is in the amplitude,  $A_s$ , due to the overall calibration shift.

**Table 18.** Constraints on the basic six-parameter  $\Lambda$ CDM model using *Planck* angular power spectra.<sup>a</sup>

Parameter	PlanckTT+lowP 68 % limits	PlanckTT,TE,EE+lowP 68 % limits
$\Omega_b h^2$ .....	$0.02222 \pm 0.00023$	$0.02225 \pm 0.00016$
$\Omega_c h^2$ .....	$0.1197 \pm 0.0022$	$0.1198 \pm 0.0015$
$100\theta_{\text{MC}}$ .....	$1.04085 \pm 0.00047$	$1.04077 \pm 0.00032$
$\tau$ .....	$0.078 \pm 0.019$	$0.079 \pm 0.017$
$\ln(10^{10} A_s)$ .....	$3.089 \pm 0.036$	$3.094 \pm 0.034$
$n_s$ .....	$0.9655 \pm 0.0062$	$0.9645 \pm 0.0049$
$H_0$ .....	$67.31 \pm 0.96$	$67.27 \pm 0.66$
$\Omega_\Lambda$ .....	$0.685 \pm 0.013$	$0.6844 \pm 0.0091$
$\Omega_m$ .....	$0.315 \pm 0.013$	$0.3156 \pm 0.0091$
$\Omega_m h^2$ .....	$0.1426 \pm 0.0020$	$0.1427 \pm 0.0014$
$\Omega_m h^3$ .....	$0.09597 \pm 0.00045$	$0.09601 \pm 0.00029$
$\sigma_8$ .....	$0.829 \pm 0.014$	$0.831 \pm 0.013$
$\sigma_8 \Omega_m^{0.5}$ .....	$0.466 \pm 0.013$	$0.4668 \pm 0.0098$
$\sigma_8 \Omega_m^{0.25}$ .....	$0.621 \pm 0.013$	$0.623 \pm 0.011$
$z_{\text{re}}$ .....	$9.9^{+1.8}_{-1.6}$	$10.0^{+1.7}_{-1.5}$
$10^9 A_s$ .....	$2.198^{+0.076}_{-0.085}$	$2.207 \pm 0.074$
$10^9 A_s e^{-2\tau}$ .....	$1.880 \pm 0.014$	$1.882 \pm 0.012$
Age/Gyr .....	$13.813 \pm 0.038$	$13.813 \pm 0.026$
$z_*$ .....	$1090.09 \pm 0.42$	$1090.06 \pm 0.30$
$r_*$ .....	$144.61 \pm 0.49$	$144.57 \pm 0.32$
$100\theta_*$ .....	$1.04105 \pm 0.00046$	$1.04096 \pm 0.00032$
$z_{\text{drag}}$ .....	$1059.57 \pm 0.46$	$1059.65 \pm 0.31$
$r_{\text{drag}}$ .....	$147.33 \pm 0.49$	$147.27 \pm 0.31$
$k_D$ .....	$0.14050 \pm 0.00052$	$0.14059 \pm 0.00032$
$z_{\text{eq}}$ .....	$3393 \pm 49$	$3395 \pm 33$
$k_{\text{eq}}$ .....	$0.01035 \pm 0.00015$	$0.01036 \pm 0.00010$
$100\theta_{\text{eq}}$ .....	$0.4502 \pm 0.0047$	$0.4499 \pm 0.0032$



**Figure 47.** CMB-only power spectra measured by *Planck* (blue), ACT (orange), and SPT (green). The best-fit PlanckTT+lowP  $\Lambda$ CDM model is shown by the grey solid line. ACT data at  $\ell > 1000$  and SPT data at  $\ell > 2000$  are marginalized CMB bandpowers from multi-frequency spectra presented in Das et al. (2013) and George et al. (2014) as extracted in this work. Lower multipole ACT ( $500 < \ell < 1000$ ) and SPT ( $650 < \ell < 3000$ ) CMB power extracted by Calabrese et al. (2013) from multi-frequency spectra presented in Das et al. (2013) and Story et al. (2012) are also shown. Note that the binned values in the range

# Cosmological parameters : a summary

- The temperature and polarization power spectra are consistent with the standard **spatially flat, six parameters,  $\Lambda$ CDM cosmology, with a power law spectrum of adiabatic scalar perturbations.**
- From the Planck temperature and lensing data Hubble constant  $H_0 = 67.8 \pm 0.9$  Km/sec/Mpc, Matter density parameter  $\Omega_m = 0.308 \pm 0.012$ , Scalar spectral index (tilt)  $n_s = 0.968 \pm 0.006$ , and Reionization optical depth  $\tau = 0.066 \pm 0.016$  and so  $z_{re} = 8.8^{1.7}_{-1.4}$ , Effective number of the relativistic degrees of freedom  $N_{\text{eff}} = 3.15 \pm 0.23$  (consistent with  $N_{\text{eff}} = 3.046$  of the standard model of particle physics), Sum of the neutrino masses  $\sum m_\nu < 0.23$ eV, Spatial curvature  $|\Omega_k| < 0.005$
- With tensor perturbations tensor to scalar ratio  $r_{0.002} < 0.11$ .

**Table 1.** Parameters of the base  $\Lambda$ CDM cosmology (as defined in PCP13) determined from the publicly released nominal-mission CamSpec DetSet likelihood [2013N(DS)] and the 2013 full-mission CamSpec DetSet and cross-yearly (Y1  $\times$  Y2) likelihoods with the extended sky coverage [2013F(DS) and 2013F(CY)]. These three likelihoods are combined with the WMAP polarization likelihood to constrain  $\tau$ . The column labelled 2015F(CHM) lists parameters for a CamSpec cross-half-mission likelihood constructed from the 2015 maps using similar sky coverage to the 2013F(CY) likelihood (but greater sky coverage at 217 GHz and different point source masks, as discussed in the text). The column labelled 2015F(CHM) (P11k) lists parameters for the Plik cross-half-mission likelihood that uses identical sky coverage to the CamSpec likelihood. The 2015 temperature likelihoods are combined with the Planck lowP likelihood to constrain  $\tau$ . The last two columns list the deviations of the Plik parameters from those of the nominal-mission and the CamSpec 2015(CHM) likelihoods. To help refer to specific columns, we have numbered the first six explicitly.

[1] Parameter	[2] 2013N(DS)	[3] 2013F(DS)	[4] 2013F(CY)	[5] 2015F(CHM)	[6] 2015F(CHM) (P11k)	([2] – [6])/ $\sigma_{[6]}$	([5] – [6])/ $\sigma_{[5]}$
$100\Omega_M$	$1.04131 \pm 0.00063$	$1.04126 \pm 0.00047$	$1.04121 \pm 0.00048$	$1.04094 \pm 0.00048$	$1.04086 \pm 0.00048$	0.71	0.17
$\Omega_b h^2$	$0.02205 \pm 0.00028$	$0.02234 \pm 0.00023$	$0.02230 \pm 0.00023$	$0.02225 \pm 0.00023$	$0.02222 \pm 0.00023$	-0.61	0.13
$\Omega_c h^2$	$0.1199 \pm 0.0027$	$0.1189 \pm 0.0022$	$0.1188 \pm 0.0022$	$0.1194 \pm 0.0022$	$0.1199 \pm 0.0022$	0.00	-0.23
$H_0$	$67.3 \pm 1.2$	$67.8 \pm 1.0$	$67.8 \pm 1.0$	$67.48 \pm 0.98$	$67.26 \pm 0.98$	0.03	0.22
$n_s$	$0.9603 \pm 0.0073$	$0.9665 \pm 0.0062$	$0.9655 \pm 0.0062$	$0.9682 \pm 0.0062$	$0.9652 \pm 0.0062$	-0.67	0.48
$\Omega_m$	$0.315 \pm 0.017$	$0.308 \pm 0.013$	$0.308 \pm 0.013$	$0.313 \pm 0.013$	$0.316 \pm 0.014$	-0.06	-0.23
$\sigma_8$	$0.829 \pm 0.012$	$0.831 \pm 0.011$	$0.828 \pm 0.012$	$0.829 \pm 0.015$	$0.830 \pm 0.015$	-0.08	-0.07
$\tau$	$0.089 \pm 0.013$	$0.096 \pm 0.013$	$0.094 \pm 0.013$	$0.079 \pm 0.019$	$0.078 \pm 0.019$	$0.85$	$0.05$
$10^9 A_s e^{-2\ell}$	$1.836 \pm 0.013$	$1.833 \pm 0.011$	$1.831 \pm 0.011$	$1.875 \pm 0.014$	$1.881 \pm 0.014$	-3.46	-0.42

**Table 2.** Goodness-of-fit tests for the 2015 *Planck* temperature and polarization spectra.  $\Delta\chi^2 = \chi^2 - N_{\text{dof}}$  is the difference from the mean assuming that the best-fit base  $\Lambda\text{CDM}$  model (fitted to *Planck* TT+lowP) is correct and  $N_{\text{dof}}$  is the number of degrees of freedom (set equal to the number of multipoles). The sixth column expresses  $\Delta\chi^2$  in units of the expected dispersion,  $\sqrt{2N_{\text{dof}}}$ , and the last column lists the probability to exceed (PTE) the tabulated value of  $\chi^2$ .

Likelihood	Frequency	Multipole range	$\chi^2$	$\chi^2/N_{\text{dof}}$	$N_{\text{dof}}$	$\Delta\chi^2 / \sqrt{2N_{\text{dof}}}$	PTE [%]
TT	100×100	30–1197	1234.37	1.06	1168	1.37	8.66
	143×143	30–1996	2034.45	1.03	1967	1.08	14.14
	143×217	30–2508	2566.74	1.04	2479	1.25	10.73
	217×217	30–2508	2549.66	1.03	2479	1.00	15.78
	Combined	30–2508	2546.67	1.03	2479	0.96	16.81
TE	100×100	30– 999	1088.78	1.12	970	2.70	0.45
	100×143	30– 999	1032.84	1.06	970	1.43	7.90
	100×217	505– 999	526.56	1.06	495	1.00	15.78
	143×143	30–1996	2028.43	1.03	1967	0.98	16.35
	143×217	505–1996	1606.25	1.08	1492	2.09	2.01
	217×217	505–1996	1431.52	0.96	1492	-1.11	86.66
	Combined	30–1996	2046.11	1.04	1967	1.26	10.47
EE	100×100	30– 999	1027.89	1.06	970	1.31	9.61
	100×143	30– 999	1048.22	1.08	970	1.78	4.05
	100×217	505– 999	479.72	0.97	495	-0.49	68.06
	143×143	30–1996	2000.90	1.02	1967	0.54	29.18
	143×217	505–1996	1431.16	0.96	1492	-1.11	86.80
	217×217	505–1996	1409.58	0.94	1492	-1.51	93.64
	Combined	30–1996	1986.95	1.01	1967	0.32	37.16

**Table 3.** Parameters of the base  $\Lambda$ CDM cosmology computed from the 2015 baseline *Planck* likelihoods illustrating the consistency of parameters determined from the temperature and polarization spectra at high multipoles. Column [1] uses the *TT* spectra at low and high multipoles and is the same as column [6] of Table 1. Columns [2] and [3] use only the *TE* and *EE* spectra at high multipoles, and only polarization at low multipoles. Column [4] uses the full likelihood. The last column lists the deviations of the cosmological parameters determined from the *TT+lowP* and *TT,TE,EE+lowP* likelihoods.

Parameter	[1] <i>Planck TT+lowP</i>	[2] <i>Planck TE+lowP</i>	[3] <i>Planck EE+lowP</i>	[4] <i>Planck TT,TE,EE+lowP</i>	$([1] - [4])/\sigma_{[1]}$
$\Omega_b h^2$ . . . . .	$0.02222 \pm 0.00023$	$0.02228 \pm 0.00025$	$0.0240 \pm 0.0013$	$0.02225 \pm 0.00016$	-0.1
$\Omega_c h^2$ . . . . .	$0.1197 \pm 0.0022$	$0.1187 \pm 0.0021$	$0.1150^{+0.0048}_{-0.0055}$	$0.1198 \pm 0.0015$	0.0
$100\theta_{\text{MC}}$ . . . . .	$1.04085 \pm 0.00047$	$1.04094 \pm 0.00051$	$1.03988 \pm 0.00094$	$1.04077 \pm 0.00032$	0.2
$\tau$ . . . . .	$0.078 \pm 0.019$	$0.053 \pm 0.019$	$0.059^{+0.022}_{-0.019}$	$0.079 \pm 0.017$	-0.1
$\ln(10^{10} A_s)$ . . . . .	$3.089 \pm 0.036$	$3.031 \pm 0.041$	$3.066^{+0.046}_{-0.041}$	$3.094 \pm 0.034$	-0.1
$n_s$ . . . . .	$0.9655 \pm 0.0062$	$0.965 \pm 0.012$	$0.973 \pm 0.016$	$0.9645 \pm 0.0049$	0.2
$H_0$ . . . . .	$67.31 \pm 0.96$	$67.73 \pm 0.92$	$70.2 \pm 3.0$	$67.27 \pm 0.66$	0.0
$\Omega_m$ . . . . .	$0.315 \pm 0.013$	$0.300 \pm 0.012$	$0.286^{+0.027}_{-0.038}$	$0.3156 \pm 0.0091$	0.0
$\sigma_8$ . . . . .	$0.829 \pm 0.014$	$0.802 \pm 0.018$	$0.796 \pm 0.024$	$0.831 \pm 0.013$	0.0
$10^9 A_s e^{-2\tau}$ . . . . .	$1.880 \pm 0.014$	$1.865 \pm 0.019$	$1.907 \pm 0.027$	$1.882 \pm 0.012$	-0.1

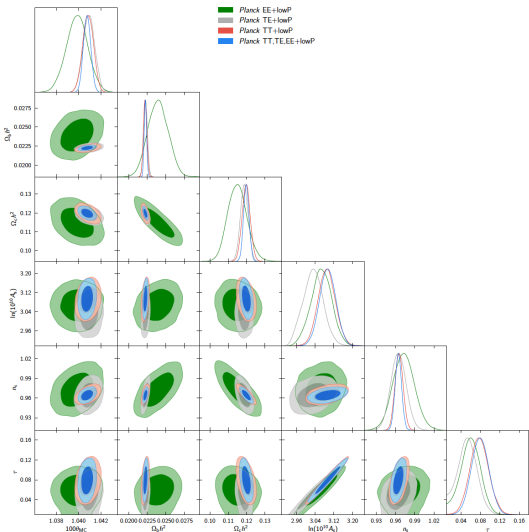
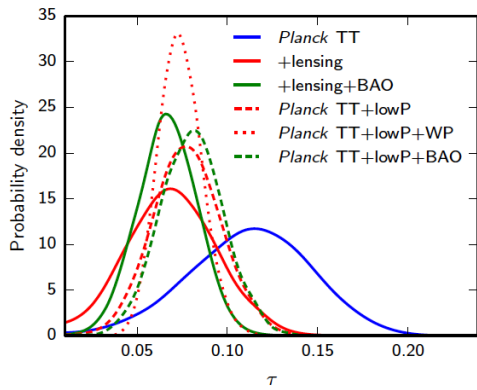
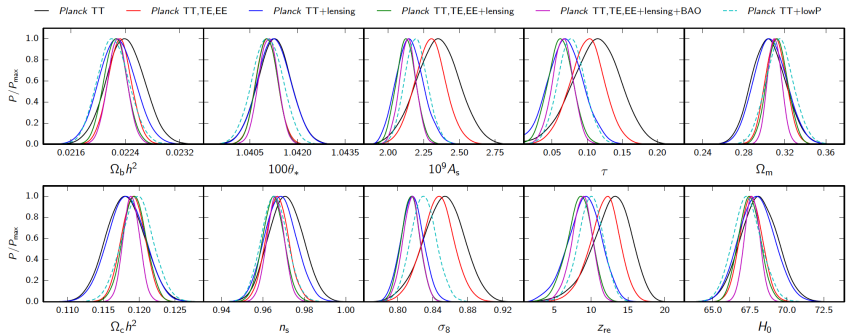


Fig. 6. Comparison of the base  $\Lambda$  $\text{CDM}$  model parameter constraints from *Planck* temperature and polarization data.



**Fig. 8.** Marginalized constraints on the reionization optical depth in the base  $\Lambda$ CDM model for various data combinations. Solid lines do not include low multipole polarization; in these cases the optical depth is constrained by *Planck* lensing. The dashed/dotted lines include LFI polarization (+lowP), or the combination of LFI and WMAP polarization cleaned using 353 GHz as a dust template (+lowP+WP).



**Fig. 7.** Marginalized constraints on parameters of the base  $\Lambda$ CDM model for various data combinations, excluding low multipole polarization, compared to the *Planck* TT+lowP constraints.

# Cosmological Parameters: Primary

**Table 4.** Parameter 68 % confidence limits for the base  $\Lambda$ CDM model from *Planck* CMB power spectra, in combination with lensing reconstruction (“lensing”) and external data (“ext,” BAO+JLA+ $H_0$ ). Nuisance parameters are not listed for brevity (they can be found in the *Planck Legacy Archive* tables), but the last three parameters give a summary measure of the total foreground amplitude (in  $\mu\text{K}^2$ ) at  $\ell = 2000$  for the three high- $\ell$  temperature spectra used by the likelihood. In all cases the helium mass fraction used is predicted by BBN (posterior mean  $Y_p \approx 0.2453$ , with theoretical uncertainties in the BBN predictions dominating over the *Planck* error on  $\Omega_b h^2$ ).

Parameter	TT+lowP 68 % limits	TT+lowP+lensing 68 % limits	TT+lowP+lensing+ext 68 % limits	TT,TE,EE+lowP 68 % limits	TT,TE,EE+lowP+lensing 68 % limits	TT,TE,EE+lowP+lensing+ext 68 % limits
$\Omega_b h^2$ . . . . .	$0.02222 \pm 0.00023$	$0.02226 \pm 0.00023$	$0.02227 \pm 0.00020$	$0.02225 \pm 0.00016$	$0.02226 \pm 0.00016$	$0.02230 \pm 0.00014$
$\Omega_c h^2$ . . . . .	$0.1197 \pm 0.0022$	$0.1186 \pm 0.0020$	$0.1184 \pm 0.0012$	$0.1198 \pm 0.0015$	$0.1193 \pm 0.0014$	$0.1188 \pm 0.0010$
$100\theta_{\text{MC}}$ . . . . .	$1.04085 \pm 0.00047$	$1.04103 \pm 0.00046$	$1.04106 \pm 0.00041$	$1.04077 \pm 0.00032$	$1.04087 \pm 0.00032$	$1.04093 \pm 0.00030$
$\tau$ . . . . .	$0.078 \pm 0.019$	$0.066 \pm 0.016$	$0.067 \pm 0.013$	$0.079 \pm 0.017$	$0.063 \pm 0.014$	$0.066 \pm 0.012$
$\ln(10^{10} A_s)$ . . . . .	$3.089 \pm 0.036$	$3.062 \pm 0.029$	$3.064 \pm 0.024$	$3.094 \pm 0.034$	$3.059 \pm 0.025$	$3.064 \pm 0.023$
$n_s$ . . . . .	$0.9655 \pm 0.0062$	$0.9677 \pm 0.0060$	$0.9681 \pm 0.0044$	$0.9645 \pm 0.0049$	$0.9653 \pm 0.0048$	$0.9667 \pm 0.0040$

# Cosmological Parameters: Derived

	$H_0$	$\Omega_A$	$\Omega_m$	$\Omega_m h^2$	$\Omega_m h^3$	$\sigma_8$	$\sigma_8 \Omega_m^{0.5}$	$\sigma_8 \Omega_m^{0.25}$	$z_{de}$	$10^9 A_s$	$10^9 A_s e^{-2r}$	Age/Gyr	$z_a$	$r_a$	$1000 r_a$	$z_{\text{drag}}$	$r_{\text{drag}}$	$k_D$	$z_{\text{eq}}$	$k_{\text{eq}}$	$1000 k_{\text{eq}}$	$f_{2000}^{143}$	$f_{2000}^{143 \times 217}$	$f_{2000}^{217}$	
	$67.31 \pm 0.96$	$0.685 \pm 0.013$	$0.315 \pm 0.013$	$0.1426 \pm 0.0020$	$0.09597 \pm 0.00045$	$0.829 \pm 0.014$	$0.466 \pm 0.013$	$0.621 \pm 0.013$	$9.9^{+1.8}_{-1.6}$	$2.198^{+0.076}_{-0.085}$	$1.880 \pm 0.014$	$13.813 \pm 0.038$	$1090.09 \pm 0.42$	$144.61 \pm 0.49$	$1.04105 \pm 0.00046$	$1059.57 \pm 0.46$	$147.33 \pm 0.49$	$0.14050 \pm 0.00052$	$3393 \pm 49$	$0.01035 \pm 0.00015$	$0.4502 \pm 0.0047$	$29.9 \pm 2.9$	$32.4 \pm 2.1$	$106.0 \pm 2.0$	
	$67.81 \pm 0.92$	$0.692 \pm 0.012$	$0.308 \pm 0.012$	$0.1415 \pm 0.0019$	$0.09591 \pm 0.00045$	$0.8149 \pm 0.0093$	$0.4521 \pm 0.0088$	$0.6069 \pm 0.0076$	$8.8^{+1.7}_{-1.4}$	$2.139 \pm 0.063$	$1.874 \pm 0.013$	$13.799 \pm 0.038$	$1089.94 \pm 0.42$	$144.89 \pm 0.44$	$1.04122 \pm 0.00045$	$1059.57 \pm 0.47$	$147.60 \pm 0.43$	$0.14024 \pm 0.00047$	$3363 \pm 44$	$0.01027 \pm 0.00014$	$0.4529 \pm 0.0044$	$30.3 \pm 2.8$	$32.7 \pm 2.0$	$106.2 \pm 2.0$	
	$67.90 \pm 0.55$	$0.6935 \pm 0.0072$	$0.3065 \pm 0.0072$	$0.1413 \pm 0.0011$	$0.09593 \pm 0.00045$	$0.8154 \pm 0.0090$	$0.4514 \pm 0.0066$	$0.6066 \pm 0.0070$	$8.9^{+1.3}_{-1.2}$	$2.143 \pm 0.051$	$1.873 \pm 0.011$	$13.796 \pm 0.029$	$1089.90 \pm 0.30$	$144.93 \pm 0.30$	$1.04126 \pm 0.00041$	$1059.60 \pm 0.44$	$147.63 \pm 0.32$	$0.14022 \pm 0.00042$	$3361 \pm 27$	$0.010258 \pm 0.000083$	$0.4533 \pm 0.0026$	$29.5 \pm 2.7$	$32.2 \pm 1.9$	$105.8 \pm 1.9$	
	$67.27 \pm 0.66$	$0.6844 \pm 0.0091$	$0.3156 \pm 0.0091$	$0.1427 \pm 0.0014$	$0.09601 \pm 0.00029$	$0.831 \pm 0.013$	$0.4668 \pm 0.0098$	$0.623 \pm 0.011$	$10.0^{+1.7}_{-1.5}$	$2.207 \pm 0.074$	$1.882 \pm 0.012$	$13.813 \pm 0.026$	$1090.06 \pm 0.30$	$144.57 \pm 0.32$	$1.04096 \pm 0.00032$	$1059.65 \pm 0.31$	$147.27 \pm 0.31$	$0.14059 \pm 0.00032$	$3395 \pm 33$	$0.01036 \pm 0.00010$	$0.4499 \pm 0.0032$	$30.2 \pm 2.7$	$32.8 \pm 1.9$	$106.2 \pm 1.9$	
	$67.51 \pm 0.64$	$0.6879 \pm 0.0087$	$0.3121 \pm 0.0087$	$0.1422 \pm 0.0013$	$0.09596 \pm 0.00030$	$0.8150 \pm 0.0087$	$0.4553 \pm 0.0068$	$0.6091 \pm 0.0067$	$8.5^{+1.4}_{-1.2}$	$2.130 \pm 0.053$	$1.878 \pm 0.011$	$13.807 \pm 0.026$	$1090.00 \pm 0.29$	$144.71 \pm 0.31$	$1.04106 \pm 0.00031$	$1059.62 \pm 0.31$	$147.41 \pm 0.31$	$0.14044 \pm 0.00032$	$3382 \pm 32$	$0.010322 \pm 0.000096$	$0.4512 \pm 0.0031$	$30.2 \pm 2.7$	$32.8 \pm 1.9$	$106.1 \pm 1.8$	
	$67.74 \pm 0.46$	$0.6911 \pm 0.0062$	$0.3089 \pm 0.0062$	$0.14170 \pm 0.00097$	$0.09598 \pm 0.00029$	$0.8159 \pm 0.0086$	$0.4535 \pm 0.0059$	$0.6083 \pm 0.0066$	$8.8^{+1.2}_{-1.1}$	$2.142 \pm 0.049$	$1.876 \pm 0.011$	$13.799 \pm 0.021$	$1089.90 \pm 0.23$	$144.81 \pm 0.24$	$1.04112 \pm 0.00029$	$1059.68 \pm 0.29$	$147.50 \pm 0.24$	$0.14038 \pm 0.00029$	$3371 \pm 23$	$0.010288 \pm 0.000071$	$0.4523 \pm 0.0023$	$30.0 \pm 2.7$	$32.6 \pm 1.9$	$106.1 \pm 1.8$	

# Cosmological Parameters: One parameter extension

**Table 5.** Constraints on 1-parameter extensions to the base  $\Lambda$ CDM model for combinations of *Planck* power spectra, *Planck* lensing, and external data (BAO+JLA+ $H_0$ , denoted “ext”). Note that we quote 95 % limits here.

Parameter	TT	TT+lensing	TT+lensing+ext	TT, TE, EE	TT, TE, EE+lensing	TT, TE, EE+lensing+ext
$\Omega_K$ .....	$-0.052^{+0.049}_{-0.055}$	$-0.005^{+0.016}_{-0.017}$	$-0.0001^{+0.0054}_{-0.0052}$	$-0.040^{+0.038}_{-0.041}$	$-0.004^{+0.015}_{-0.015}$	$0.0008^{+0.0040}_{-0.0039}$
$\Sigma m_\nu$ [eV] .....	$< 0.715$	$< 0.675$	$< 0.234$	$< 0.492$	$< 0.589$	$< 0.194$
$N_{\text{eff}}$ .....	$3.13^{+0.64}_{-0.63}$	$3.13^{+0.62}_{-0.61}$	$3.15^{+0.41}_{-0.40}$	$2.99^{+0.41}_{-0.39}$	$2.94^{+0.38}_{-0.38}$	$3.04^{+0.33}_{-0.33}$
$Y_P$ .....	$0.252^{+0.041}_{-0.042}$	$0.251^{+0.040}_{-0.039}$	$0.251^{+0.035}_{-0.036}$	$0.250^{+0.026}_{-0.027}$	$0.247^{+0.026}_{-0.027}$	$0.249^{+0.025}_{-0.026}$
$dn_s/d \ln k$ .....	$-0.008^{+0.016}_{-0.016}$	$-0.003^{+0.015}_{-0.015}$	$-0.003^{+0.015}_{-0.014}$	$-0.006^{+0.014}_{-0.014}$	$-0.002^{+0.013}_{-0.013}$	$-0.002^{+0.013}_{-0.013}$
$r_{0.002}$ .....	$< 0.103$	$< 0.114$	$< 0.114$	$< 0.987$	$< 0.112$	$< 0.113$
$w$ .....	$-1.54^{+0.62}_{-0.50}$	$-1.41^{+0.64}_{-0.56}$	$-1.006^{+0.085}_{-0.091}$	$-1.55^{+0.58}_{-0.48}$	$-1.42^{+0.62}_{-0.56}$	$-1.019^{+0.075}_{-0.080}$

# Scalar Spectral Index

## 6.2.1. Scalar spectral index and tensor fluctuations

Primordial tensor fluctuations (gravitational waves) contribute to both the CMB temperature and polarization power spectra. Gravitational waves entering the horizon between recombination and the present day generate a tensor contribution to the large-scale CMB temperature anisotropy. In this data release, the strongest constraint on tensor modes from *Planck* data still comes from the CMB temperature spectrum at  $\ell \lesssim 100$ . The corresponding comoving wavenumbers probed by the *Planck* temperature spectrum have  $k \lesssim 0.008 \text{ Mpc}^{-1}$ , with very little sensitivity to higher wavenumbers because gravitational waves decay on sub-horizon scales. The precision of the *Planck* constraint is

---

<sup>21</sup>The pivot scale quoted here is roughly appropriate for the scales probed by BICEP2.

# Scalar Spectral Index

limited by cosmic variance of the dominant scalar anisotropies, and it is also model dependent. In polarization, in addition to  $B$ -modes, the  $EE$  and  $TE$  spectra also contain a signal from tensor modes coming from reionization and last scattering. However, in this release the addition of *Planck* polarization constraints at  $\ell \geq 30$  do not significantly change the results from temperature and low- $\ell$  polarization (see Table 5).

Figure 21 shows the 2015 *Planck* constraint in the  $n_s$ – $r$  plane, adding  $r$  as a one-parameter extension to base  $\Lambda\text{CDM}$ . Note that for base  $\Lambda\text{CDM}$  ( $r = 0$ ), the value of  $n_s$  is

$$n_s = 0.9655 \pm 0.0062, \quad \text{Planck TT+lowP.} \quad (38)$$

We highlight this number here since  $n_s$ , a key parameter for inflationary cosmology, shows one of the largest shifts of any parameter in base  $\Lambda\text{CDM}$  between the *Planck* 2013 and *Planck* 2015 analyses (about  $0.7\sigma$ ). As explained in Sect. 3.1, part of this shift was caused by the  $\ell \approx 1800$  systematic in the nominal-mission  $217 \times 217$  spectrum used in PCP13.

The red contours in Fig. 21 show the constraints from *Planck* TT+lowP. These are similar to the constraints shown in Fig. 23 of PCP13, but with  $n_s$  shifted to slightly higher values. The addition of BAO or the *Planck* lensing data to Planck TT+lowP lowers the value of  $\Omega_bh^2$ , which at fixed  $\theta_s$  increases the small-scale CMB power. To maintain the fit to the *Planck* temperature power spectrum for models with  $r = 0$ , these parameter shifts are compensated by a change in amplitude  $A_s$  and the tilt  $n_s$  (by about  $0.4\sigma$ ). The increase in  $n_s$  to match the observed power on small scales leads to a decrease in the scalar power on large scales, allowing room for a slightly larger contribution

from tensor modes. The constraints shown by the blue contours in Fig. 21, which add *Planck* lensing, BAO, and other astrophysical data, are therefore tighter in the  $n_s$  direction and shifted to slightly higher values, but marginally weaker in the  $r$ -direction. The 95 % limits on  $r_{0.002}$  are

$$r_{0.002} < 0.10, \quad \text{Planck TT+lowP,} \quad (39a)$$

$$r_{0.002} < 0.11, \quad \text{Planck TT+lowP+lensing+ext,} \quad (39b)$$

consistent with the results reported in PCP13. Note that we assume the second-order slow-roll consistency relation for the tensor spectral index. The result in Eqs. (39a) and (39b) are mildly scale dependent, with equivalent limits on  $r_{0.05}$  being weaker by about 5 %.

PCP13 noted a mismatch between the best-fit base  $\Lambda\text{CDM}$  model and the temperature power spectrum at multipoles  $\ell \lesssim 40$ , partly driven by the dip in the multipole range  $20 \leq \ell \lesssim 30$ . If this mismatch is simply a statistical fluctuation of the  $\Lambda\text{CDM}$  model (and there is no compelling evidence to think otherwise), the strong *Planck* limit (compared to forecasts) is the result of chance low levels of scalar mode confusion. On the other hand if the dip represents a failure of the  $\Lambda\text{CDM}$  model, the 95 % limits of Eqs. (39a) and (39b) may be underestimates. These issues are considered at greater length in [Planck Collaboration XX \(2015\)](#) and will not be discussed further in this paper.

As mentioned above, the *Planck* temperature constraints on  $r$  are model-dependent and extensions to  $\Lambda\text{CDM}$  can give significantly different results. For example, extra relativistic degrees of freedom increase the small-scale damping of the CMB anisotropies at a fixed angular scale, which can be compensated

# Scalar Spectral Index

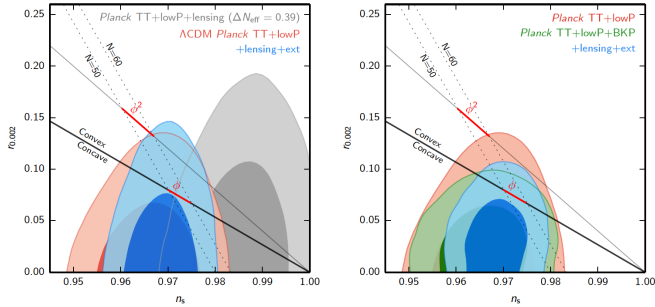


**Fig. 21.** *Left:* Constraints on the tensor-to-scalar ratio  $r_{0.002}$  in the  $\Lambda\text{CDM}$  model, using *Planck* TT+lowP and *Planck* TT+lowP+lensing+BAO+JLA+ $H_0$  (red and blue, respectively) assuming negligible running and the inflationary consistency relation. The result is model-dependent; for example, the grey contours show how the results change if there were additional relativistic degrees of freedom with  $\Delta N_{\text{eff}} = 0.39$  (disfavoured, but not excluded, by *Planck*). Dotted lines show loci of approximately constant  $e$ -folding number  $N$ , assuming simple  $V \propto (\phi/m_p)^p$  single-field inflation. Solid lines show the approximate  $n_s$ - $r$  relation for quadratic and linear potentials to first order in slow roll; red lines show the approximate allowed range assuming  $50 < N < 60$  and a power-law potential for the duration of inflation. The solid black line (corresponding to a linear potential) separates concave and convex potentials. *Right:* Equivalent constraints in the  $\Lambda\text{CDM}$  model when adding  $B$ -mode polarization results corresponding to the default configuration of the BICEP2/Keck Array+*Planck* (BKP) likelihood. These exclude the quadratic potential at a higher level of significance compared to the *Planck*-alone constraints.

# Dark matter

## 6.6. Dark matter annihilation

Energy injection from dark matter (DM) annihilation can alter the recombination history, leading to changes in the temperature and polarization power spectra of the CMB (e.g., [Chen & Kamionkowski 2004](#); [Padmanabhan & Finkbeiner 2005](#)). As demonstrated in several papers (e.g., [Galli et al. 2009](#); [Slatyer et al. 2009](#); [Finkbeiner et al. 2012](#)), CMB anisotropies offer the opportunity to constrain the nature of DM. Furthermore, CMB experiments such as *Planck* can achieve limits on the annihilation cross-section that are relevant to the interpretation of the rise in the cosmic-ray positron fraction at energies  $\gtrsim 10$  GeV observed by PAMELA, *Fermi*, and AMS ([Adriani et al. 2009](#); [Ackermann et al. 2012](#); [Aguilar et al. 2014](#)). The CMB constraints are complementary to those determined from other astrophysical probes, such as the gamma-ray observations of dwarf galaxies by the *Fermi* satellite ([Ackermann et al. 2014](#)).

# Dark Matter

The way in which DM annihilations heat and ionize the gaseous background depends on the nature of the cascade of particles produced following annihilation and, in particular, on the production of  $e^\pm$  pairs and photons that couple to the gaseous background. The fraction of the rest mass energy that is injected into the gaseous background can be modelled by an “efficiency factor”,  $f(z)$ , which is typically in the range  $f = 0.01\text{--}1$  and depends on redshift<sup>28</sup>. Computations of  $f(z)$  for various annihilation channels can be found in Slatyer et al. (2009), Hutsi et al. (2009) and Evoli et al. (2013). The rate of energy release per unit volume by annihilating DM can therefore be written as

$$\frac{dE}{dt dV}(z) = 2g \rho_{\text{crit}}^2 c^2 \Omega_c^2 (1+z)^6 p_{\text{ann}}(z), \quad (80)$$

where  $p_{\text{ann}}$  is defined as

$$p_{\text{ann}}(z) \equiv f(z) \frac{\langle \sigma v \rangle}{m_\chi}, \quad (81)$$

$\rho_{\text{crit}}$  the critical density of the Universe today,  $m_\chi$  is the mass of the DM particle, and  $\langle \sigma v \rangle$  is the thermally-averaged annihilation cross-section times (Möller) velocity (we will refer to this quantity loosely as the “cross-section” hereafter). In Eq. (80),  $g$  is a degeneracy factor that is equal to 1/2 for Majorana particles and 1/4 for Dirac particles. In this paper, the constraints will refer to Majorana particles. Note that to produce the observed dark matter density from thermal DM relics requires an s-wave annihilation cross-section of  $\langle \sigma v \rangle \approx 3 \times 10^{-26} \text{ cm}^3 \text{ s}^{-1}$  at the time of freeze-out (see e.g., the review by Profumo 2013).

Both the amplitude and redshift dependence of the efficiency factor  $f(z)$  depend on the details of the annihilation process (e.g., Slatyer et al. 2009). The functional shape of  $f(z)$  can be taken into account using generalized parameterizations or principal components (Finkbeiner et al. 2012; Hutsi et al. 2011), similar to the analysis of the recombination history presented in Sect. 6.7.4. However, as shown in Galli et al. (2011), Giesen et al. (2012), and Finkbeiner et al. (2012), to a first approximation the redshift dependence of  $f(z)$  can be ignored, since current CMB data (including *Planck*) are sensitive to energy injection over a relatively narrow range of redshift, typically  $z \approx 1000\text{--}600$ . The effects of DM annihilation can therefore be reasonably well parameterized by a single constant parameter,  $p_{\text{ann}}$ , (with  $f(z)$  set to a constant  $f_{\text{eff}}$ ) that encodes the dependence on the properties of the DM particles. In the following, we calculate constraints on the  $p_{\text{ann}}$  parameter, assuming that it is constant, and then project these constraints on to a particular dark matter model assuming  $f_{\text{eff}} = f(z=600)$ , since the effect of dark matter annihilation peaks at  $z \approx 600$  (see Finkbeiner et al. 2012). The  $f(z)$  functions used here are those calculated in Slatyer et al. (2009), with the updates described in Galli et al. (2013) and Madhavacheril et al. (2014). Finally, we estimate the fractions of injected energy that affect the gaseous background, from heating, ionizations, or Ly $\alpha$  excitations using the updated calculations described in Galli et al. (2013) and Valdes et al. (2010), following Shull & van Steenberg (1985).

We compute the theoretical angular power in the presence of DM annihilations by modifying the `recfast` routine (Seager et al. 1999) in the `camb` code as in Galli et al. (2011).<sup>29</sup>

# Dark matter

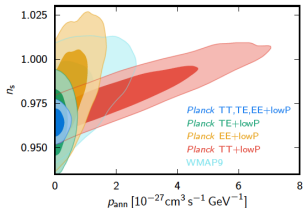


**Fig. 40.** 2-dimensional marginal distributions in the  $p_{\text{ann}}-n_s$  plane for *Planck* TT+lowP (red), EE+lowP (yellow), TE+lowP (green), and *Planck* TT,TE,EE+lowP (blue) data combinations. We also show the constraints obtained using WMAP9 data (light blue).

We then add  $p_{\text{ann}}$  as an additional parameter to those of the base  $\Lambda\text{CDM}$  cosmology. Table 6 shows the constraints for various data combinations.

**Table 6.** Constraints on  $p_{\text{ann}}$  in units of  $\text{cm}^3 \text{ s}^{-1} \text{ GeV}^{-1}$ .

Data combinations	$p_{\text{ann}}$ (95 % upper limits)
TT+lowP	$< 5.7 \times 10^{-27}$
EE+lowP	$< 1.4 \times 10^{-27}$
TE+lowP	$< 5.9 \times 10^{-28}$
TT+lowP+lensing	$< 4.4 \times 10^{-27}$
TT,TE,EE+lowP	$< 4.1 \times 10^{-28}$
TT,TE,EE+lowP+lensing	$< 3.4 \times 10^{-28}$

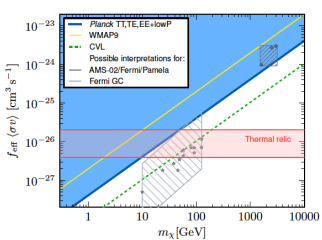


**Fig. 41.** Constraints on the self-annihilation cross-section at recombination,  $\langle\sigma v\rangle_z$ , times the efficiency parameter,  $f_{\text{eff}}$  (Eq. 81). The blue area shows the parameter space excluded by the *Planck* TT,TE,EE+lowP data at 95 % CL. The yellow line indicates the constraint using WMAP9 data. The dashed green line delineates the region ultimately accessible by a cosmic variance limited experiment with angular resolution comparable to that of *Planck*. The horizontal red band includes the values of the thermal-relic cross-section multiplied by the appropriate  $f_{\text{eff}}$  for different DM annihilation channels. The dark grey circles show the best-fit DM models for the PAMELA/AMS-02/*Fermi* cosmic-ray excesses, as calculated in Cholis & Hooper (2013) (caption of their figure 6). The light grey stars show the best-fit DM models for the *Fermi* Galactic centre gamma-ray excess, as calculated by Calore et al. (2014) (their tables I, II, and III), with the light grey area indicating the astrophysical uncertainties on the best-fit cross-sections.

improvement if other astrophysical data, or *Planck* lensing, are added.<sup>30</sup>

We verified the robustness of the *Planck* TT,TE,EE+lowP

# References

- ① Planck 2015 results. I. Overview of products and scientific results  
[arXiv:1502.01582 [astro-ph.CO]]
- ② Planck 2015 results. XI. CMB power spectra, likelihoods, and robustness of parameters [arXiv:1507.02704 [astro-ph.CO]]
- ③ Planck 2015 results. XIII. Cosmological parameters [arXiv:1502.01589 [astro-ph.CO]]